

Cellular Sensing Governs the Stability of Chemotactic Fronts

Ricard Alert,^{1,2,3,4,*} Alejandro Martínez-Calvo,^{1,5} and Sujit S. Datta^{5,†}

¹Princeton Center for Theoretical Science, Princeton University, Princeton, NJ 08544, USA

²Lewis-Sigler Institute for Integrative Genomics, Princeton University, Princeton, NJ 08544, USA

³Max Planck Institute for the Physics of Complex Systems, Nöthnitzerstr. 38, 01187 Dresden, Germany

⁴Center for Systems Biology Dresden, Pfotenhausstr. 108, 01307 Dresden, Germany

⁵Department of Chemical and Biological Engineering, Princeton University, Princeton, NJ 08544, USA

(Dated: June 7, 2022)

In contexts ranging from embryonic development to bacterial ecology, cell populations migrate chemotactically along self-generated chemical gradients, often forming a propagating front. Here, we theoretically show that the stability of such chemotactic fronts to morphological perturbations is determined by limitations in the ability of individual cells to sense and thereby respond to the chemical gradient. Specifically, cells at bulging parts of a front are exposed to a smaller gradient, which slows them down and promotes stability, but they also respond more strongly to the gradient, which speeds them up and promotes instability. We predict that this competition leads to chemotactic fingering when sensing is limited at too low chemical concentrations. Guided by this finding and by experimental data on *E. coli* chemotaxis, we suggest that the cells' sensory machinery might have evolved to avoid these limitations and ensure stable front propagation. Finally, as sensing of any stimuli is necessarily limited in living and active matter in general, the principle of sensing-induced stability may operate in other types of directed migration such as durotaxis, electrotaxis, and phototaxis.

Fronts are propagating interfaces that allow one spatial domain to invade another. They are ubiquitous in nature, arising for example during phase transitions, autocatalytic chemical reactions, and flame propagation^{1–6}. Biology also abounds with examples, such as fronts of gene expression during development, electric signals in the heart and the brain, infection during disease outbreaks, and expanding populations in ecosystems^{7–9}. These examples can all be modeled as reaction-diffusion systems (e.g., using the Fisher-KPP equation^{10,11}), for which both the motion and morphologies of fronts are well understood^{1–6}.

Another prominent and separate class of fronts is that of *chemotactic fronts*, in which active agents collectively migrate in response to a self-generated chemical gradient. These fronts have long been observed in bacterial populations, enabling cells to escape from harmful conditions, colonize new terrain, and coexist^{12–21}. More generally, collective chemotaxis plays crucial roles in slime mold aggregation²², embryonic development^{23–25}, immune response²⁶, and cancer progression^{27,28}. Beyond cell populations, enzymes^{29–31} and synthetic active colloids^{32–34} also exhibit collective chemotaxis. Therefore, studies of chemotactic fronts are of broad interest in biological and active matter physics. However, while the motion of chemotactic fronts can be successfully modeled in certain cases^{17,18,20,21,35–39}, a general understanding of how their morphologies evolve – akin to that of reaction-diffusion systems – remains lacking.

For example, a fundamental feature of a front is its morphological stability: Do shape perturbations decay or grow over time? This question is well-studied in non-living systems. In many cases, flat fronts are unstable, leading to striking dendritic patterns at fluid and solid interfaces as in the case of the well-studied Saffman-Taylor and

Mullins-Sekerka instabilities^{6,40–46}. In active and living matter, front instabilities underlie fingering patterns in active colloids⁴⁷, growing tumors^{48,49} and bacterial biofilms^{50–60}, as well as mechanically-competing tissues^{61,62} and spreading epithelia^{63–66}. Front stability has also been analyzed when chemotaxis supplements effects like growth and mechanical interactions^{37,50,67–69}.

Nevertheless, the conditions for the stability of chemotactic fronts remain unknown. Unlike reaction-diffusion systems, which rely only on scalar couplings between fields, chemotaxis couples the population density to the *gradient* of a chemical signal. Thus, the analytical techniques used to study the stability of reaction-diffusion fronts⁴ cannot be directly applied to their chemotactic counterparts⁷⁰.

Here, through direct analysis of their governing equations, we determine the conditions for the linear stability of chemotactic cell fronts. We find that front stability is determined by the ability of cells to sense chemical stimuli at different concentrations, which modulates their response to the chemical gradient and subsequent propagation speeds at different locations along the front. Our calculations reveal two competing mechanisms governing front stability: When cells move ahead of the front, they absorb chemoattractant, causing follower cells to be exposed to (i) a smaller chemical gradient, which slows cells down and promotes stability, and (ii) a lower chemical concentration, which increases the cellular response, speeds cells up, and promotes instability. We predict a chemotactic fingering instability when sensing is limited at low chemical concentrations, for which the tactic response is strong. Therefore, our work links the properties of the sensory machinery of individual cells to the population-scale morphology of chemotactic fronts. Finally, we suggest that this machinery might have evolved to push sensing limitations to high chemical concentrations in order to ensure stable collective chemotaxis.

Keller-Segel equations. Following classic work by Keller and Segel^{35,36}, we model chemotactic fronts through the cou-

* ricard.alert@princeton.edu

† ssdatta@princeton.edu

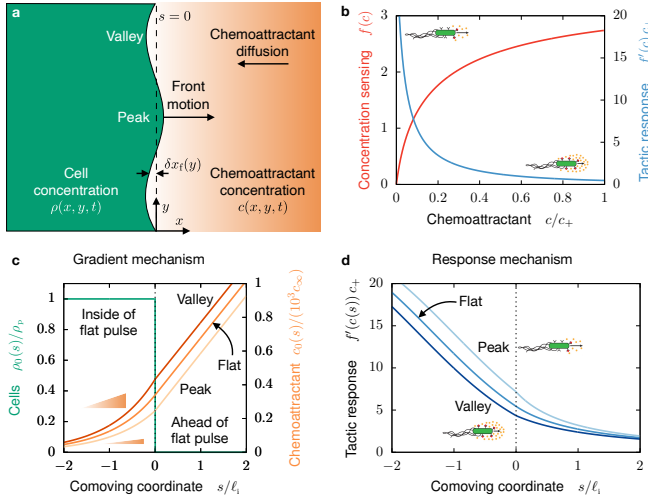


Figure 1 | Competing mechanisms of chemotactic front stability.

a, Schematic of a cell population (green) moving up a chemoattractant gradient (orange). We analyze the stability of a reference flat front (dashed line, located at the origin of the comoving coordinate $s \equiv x - v_0 t = 0$) to perturbations $\delta x_f(y)$, which create peaks and valleys. Note that we did not represent the y -dependence of the chemoattractant field. **b**, Whereas the ability of cells to sense chemoattractant, $f(c)$, increases with chemoattractant concentration, their tactic response to gradients, $f'(c)$, decreases. **c**, Assuming a step profile of cells (green), the chemoattractant profiles for the reference flat front (Eq. (3)) as well as for peaks and valleys of a perturbed front are shown by the orange curves. The comoving coordinate is rescaled by the internal decay length ℓ_i (see text). As depicted in the insets, the chemoattractant gradient at $s = 0$ is higher in valleys and lower in peaks, favoring front stability (first term in Eq. (4)). **d**, As depicted in the insets, the cellular response at $s = 0$ is stronger in peaks and weaker in valleys, favoring instability (second term in Eq. (4)). In **c** and **d**, we used front perturbations $\delta x_f(y) = \delta A \sin(ky)$ with amplitude $\delta A = 2 \mu\text{m}$ and wavelength $\lambda = 2\pi/k = 2 \text{ mm}$. Parameter values are in Table I.

pled dynamics of a chemoattractant (concentration c), which has diffusivity D_c and is absorbed by each cell at a maximal rate k , and cells (concentration ρ), which bias their motion in response to a sensed chemoattractant gradient (Fig. 1a):

$$\partial_t c = D_c \nabla^2 c - k \rho g(c). \quad (1)$$

$$\partial_t \rho = -\nabla \cdot \mathbf{J}; \quad \mathbf{J} = -D_\rho \nabla \rho + \rho \chi \nabla f(c). \quad (2)$$

Here, $g(c)$ describes how chemoattractant uptake is limited by its availability, modeled using Michaelis-Menten kinetics as $g(c) = c/(c + c_M)$ with half-maximum concentration c_M . The cell concentration evolves through the flux \mathbf{J} , which has a diffusive contribution arising from undirected motion with an effective diffusivity D_ρ , and a chemotactic contribution arising from directed motion up the chemical gradient with a drift velocity $v_c = \chi \nabla f(c)$. The function $f(c)$ characterizes the ability of cells to sense the chemoattractant. For illustration purposes, we use the established logarithmic sensing function^{17,18,71} $f(c) = \ln\left(\frac{1+c/c_-}{1+c/c_+}\right)$, with lower and upper

characteristic concentrations c_- and c_+ (Fig. 1b, red). The chemotactic coefficient χ describes the ability of the cells to migrate up the sensed chemoattractant gradient. In what follows, we determine front stability in terms of $f'(c) > 0$ and $f''(c) < 0$, regardless of the specific form of $f(c)$. Hence, our results can be generalized to other active systems employing different forms of sensing that also typically increase and eventually saturate with increasing stimulus.

While additional details (e.g., other chemicals, cellular proliferation) can also be introduced, here we focus on the minimal model of chemotactic fronts. Indeed, in excellent agreement with experiments, Eqs. (1) and (2) give rise to a propagating pulse of cells^{17,18,20,36,38}. However, the full Eqs. (1) and (2) cannot be solved analytically, precluding a generic analysis of front stability.

Flat front. To overcome this issue, we follow earlier work⁵⁷ and consider a simplified description of the pulse as a step profile with cell concentration ρ_p moving along the \hat{x} axis at speed v_0 : $\rho_0(s) = \rho_p \theta(-s)$ (Fig. 1c, green). Here, $s \equiv x - v_0 t$ is the comoving coordinate, and θ is the Heaviside step function. We discuss the validity of this approximation in the SI. The front of the pulse, located at $s = 0$, is taken to be flat, i.e. independent of the transverse coordinate y (dashed line in Fig. 1a). Ahead of the pulse ($s > 0$), there are no cells, and hence no chemoattractant absorption. Inside the pulse ($s < 0$), chemoattractant is absorbed; we assume that its concentration is smaller or similar to c_M , and hence we approximate $g(c) \approx c/c_M$, whose validity we verify *a posteriori* using our parameter estimates (Table I). We impose boundary conditions $c(s \rightarrow -\infty) = 0$ and $c(s \rightarrow \infty) = c_\infty$, with c_∞ being the chemoattractant concentration far ahead of the front, and we require continuity of the chemoattractant concentration and flux at the front.

We thereby obtain the traveling chemoattractant profile $c_0(s)$ (Fig. 1c, orange):

$$c_0^a(s) = c_\infty \left[1 - \frac{\sqrt{1+4\Gamma}-1}{\sqrt{1+4\Gamma}+1} \exp\left[-\frac{s}{\ell_d}\right] \right]; \quad s \geq 0, \quad (3a)$$

$$c_0^i(s) = \frac{2c_\infty}{\sqrt{1+4\Gamma}+1} \exp\left[\frac{s}{2\ell_d} \left(\sqrt{1+4\Gamma}-1\right)\right]; \quad s \leq 0. \quad (3b)$$

Ahead of the pulse (Eq. (3a)), the chemoattractant concentration varies exponentially over a diffusion length scale $\ell_d \equiv D_c/v_0$, which results from the balance of front motion and chemoattractant diffusion. Inside the pulse (Eq. (3b)), chemoattractant decays over a different, internal length scale $\ell_i \equiv \sqrt{\ell_d \ell_a} \equiv \ell_d/\sqrt{\Gamma}$, where the absorption length $\ell_a \equiv v_0 c_M / (k \rho_p)$ results from the balance of front motion and chemoattractant absorption. We have also defined the dimensionless parameter $\Gamma \equiv \ell_d/\ell_a$, which we call the diffusio-absorption number. Representative values of all these parameters are given in Table I.

Front perturbations. We next analyze the linear stability of this front against morphological perturbations. We perturb the cell concentration profile along the \hat{y} axis, transverse to the propagation direction: $\rho(x, y, t) = \rho_0(s - \delta x_f(y, t))$,

where $\delta x_f(y, t)$ represents the perturbation in front position (**Fig. 1a**). Consequently, the chemoattractant field is perturbed as $c(x, y, t) = c_0(s) + \delta c(s, y, t)$. For perturbations of wave number q , the chemoattractant field relaxes at a rate $\sim D_c q^2$ according to [Eq. \(1\)](#). We assume $D_c \gg D_\rho$, as is the case for cells migrating in porous media or on substrates. In this limit, chemoattractant perturbations rapidly reach a quasi-stationary profile $\delta c(s, y)$ that adapts to the slowly-evolving cell front ([SI](#)).

The cell front moves by diffusion and chemotaxis ([Eq. \(2\)](#)). As expected, the diffusive flux $-D_\rho \nabla \rho$ tends to stabilize the front by smoothing out transverse gradients of cell concentration. The influence of the chemotactic drift flux ρv_c , however, is more subtle. To gain intuition, we express the chemotactic velocity as $v_c = \chi \nabla f(c) = \chi f'(c) \nabla c$. As in linear response theory, v_c can be viewed as the cellular response to the driving force given by the chemoattractant gradient, ∇c , with $\chi f'(c)$ being the response function. Whereas the sensing ability $f(c)$ increases with chemoattractant concentration, the tactic response $f'(c)$ decreases as sensing becomes increasingly saturated (**Fig. 1b**). Because v_c involves the product of $f'(c)$ and ∇c , its perturbation has two contributions, $\delta v_c = \chi [f'(c) \nabla \delta c + \delta f'(c) \nabla c]$, which correspond to perturbations of the gradient and the response, respectively.

Competing mechanisms of front stability. How do these distinct contributions affect front stability? In a linear stability analysis, to first order in perturbations, front motion depends on the chemotactic velocity perturbation δv_c evaluated at the position of the unperturbed front, $s = 0$. While this perturbation has components both in the transverse (\hat{y}) and the propagation (\hat{x}) directions, as we show in the full analysis in the [SI](#), front stability is determined by the sign of the \hat{x} component,

$$\delta v_{c,x}(s = 0, y) = \chi [f'_0 \partial_s \delta c(0, y) + \partial_s c_0(0) f''_0 \delta c(0, y)]. \quad (4)$$

Here, we have used $\delta f'(c) = f''(c) \delta c$ and expressed dependencies on x via the comoving coordinate $s = x - v_0 t$; $c_0(s)$ is given by [Eq. \(3\)](#).

The first contribution in [Eq. \(4\)](#) is given by changes in the chemoattractant gradient at the position of the unperturbed front, $\partial_s \delta c(0, y)$, multiplied by the unperturbed chemotactic response, $f'_0 \equiv f'(c_0(0)) > 0$. We name this contribution the *gradient mechanism*; it represents changes in cell velocity due to spatial variations in the driving force ∇c . Specifically, in peaks of the perturbed front ($\delta x_f(y) > 0$), cells populate the position of the unperturbed front ($s = 0$), thereby absorbing chemoattractant and decreasing its concentration: $\delta c(0, y) < 0$ (compare peak and flat in **Fig. 1c**). As a result, the chemoattractant gradient inside the pulse ($s < 0$) decreases with respect to the unperturbed situation (**Fig. 1c**), and thus $\partial_s \delta c(0, y) < 0$. Because this first contribution in [Eq. \(4\)](#) is negative, it is stabilizing. Intuitively, the decrease in chemoattractant gradient slows down cells in peaks, allowing the rest of the population to catch up and flatten the front.

The second contribution in [Eq. \(4\)](#) is given by the unperturbed chemoattractant gradient, $\partial_s c_0(0) > 0$, multiplied by the change in the chemotactic response at the front, $\delta f'(c) = f''_0 \delta c$, where $f''_0 \equiv f''(c_0(0)) < 0$ (**Fig. 1b**). We name this contribution the *response mechanism*; it represents changes in

cell velocity due to spatial variations in the cells' chemotactic response. As noted above, in peaks of the perturbed front ($\delta x_f(y) > 0$), cells absorb chemoattractant and decrease its concentration at $s = 0$, giving $\delta c(0, y) < 0$. Because this second contribution in [Eq. \(4\)](#) is positive, it is destabilizing. Intuitively, the decrease in chemoattractant causes cells in peaks to respond to the gradient more strongly (compare peak and flat in **Fig. 1d**) and move faster, leaving the rest of the population behind and amplifying front perturbations.

Thus, our analysis reveals two competing chemotactic mechanisms that determine front stability: Cells at a bulging part of the front are exposed to a smaller chemoattractant gradient, which slows them down (gradient mechanism), but they respond more strongly to the gradient, which speeds them up (response mechanism). To quantitatively compare these two mechanisms, we rewrite [Eq. \(4\)](#) as $\delta v_{c,x}(s = 0, y) = \chi \left[\alpha \partial_s - \beta \frac{c'_0(0)}{c_\infty} \right] \frac{\delta c(0, y)}{c_\infty}$, where the two positive dimensionless parameters $\alpha \equiv f'_0 c_\infty$ and $\beta \equiv -f''_0 c_\infty^2$ quantify the strengths of the gradient and response mechanisms, respectively.

Chemotactic fingering instability. Having identified the two mechanisms whereby chemotaxis influences front stability, we solve the full [Eq. \(2\)](#) to obtain front speed perturbations $\delta v(y, t) = \partial_t \delta x_f(y, t)$ ([Eq. \(S14\)](#)), and hence the growth rate $\omega(q) \equiv \tilde{\delta v}(q)/\tilde{\delta x}_f(q)$ of front perturbations with wave number q , where tildes indicate Fourier components ([SI](#)):

$$\begin{aligned} \omega(q) = & -D_\rho q^2 + \frac{\chi}{\ell_d^2} \frac{\sqrt{1+4\Gamma}-1}{\sqrt{1+4q^2\ell_d^2}+\sqrt{1+4(\Gamma+q^2\ell_d^2)}} \\ & \times \left[\beta \frac{\sqrt{1+4\Gamma}-1}{\sqrt{1+4\Gamma}+1} - \frac{\alpha}{2} \left(\sqrt{1+4(\Gamma+q^2\ell_d^2)} - 1 \right) \right. \\ & \left. - 2\alpha \frac{q^2\ell_d^2}{\sqrt{1+4(\Gamma+q^2\ell_d^2)}-1} \right]. \end{aligned} \quad (5)$$

Fig. 2a shows this growth rate separating the contributions of the different mechanisms. As expected, the diffusive contribution $-D_\rho q^2$ is always stabilizing (**Fig. 2a**, green). At large length scales (small q), it is negligible in front of the two chemotactic mechanisms resulting from [Eq. \(4\)](#). In agreement with our argument above, the *gradient mechanism* ($\propto \alpha$ in [Eq. \(5\)](#)) is stabilizing (**Fig. 2a**, orange), while the *response mechanism* ($\propto \beta$ in [Eq. \(5\)](#)) is destabilizing (**Fig. 2a**, blue). In the long-wavelength limit ($q \rightarrow 0$), we have $\omega(0) = \frac{\chi}{\ell_d^2} \left(\frac{\sqrt{1+4\Gamma}-1}{\sqrt{1+4\Gamma}+1} \right)^2 [\beta - \frac{\alpha}{2} (\sqrt{1+4\Gamma}+1)]$, and hence the flat front becomes unstable, $\omega(0) > 0$, if

$$\beta > \frac{\alpha}{2} \left(\sqrt{1+4\Gamma} + 1 \right), \quad (6)$$

i.e. if the chemotactic response decreases too strongly with chemoattractant concentration, corresponding to large values of β . In this case, cells at valleys, which are exposed to higher concentrations, respond too weakly and are left behind by cells at peaks, which are instead exposed to lower concentrations and thus respond more strongly to the gradient.

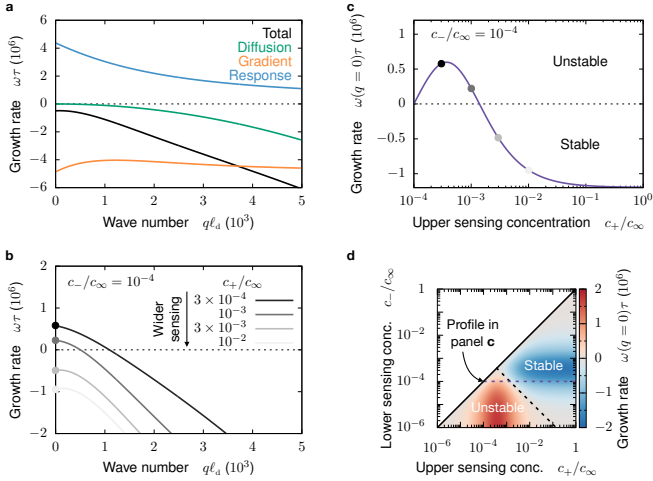


Figure 2 | Cellular sensing governs chemotactic front stability. **a**, Growth rate of front perturbations, showing the contributions of cell diffusion as well as the gradient and response chemotactic mechanisms (see Figs. 1c and 1d). **b**, Increasing the upper sensing concentration c_+ promotes front stability. **c**, As sensing becomes less limited at higher concentrations by increasing c_+ , the front can switch from unstable to stable, as indicated by the sign of the long-wavelength growth rate $\omega(q = 0)$. The points correspond to those in panel b. **d**, Diagram of front stability as a function of the lower and upper characteristic sensing concentrations. The color code informs about the degree of front stability, as given by $\omega(q = 0)$. The black dashed line indicates the stability limit (Eq. (7)). The purple dashed line indicates the slice of the diagram shown in panel c. Throughout the figure, the growth rate is rescaled by what we call the chemotactic time $\tau \equiv \ell_d^2/\chi$. Parameter values are in Table I.

Cellular sensing governs chemotactic front stability. Our central result, given by Eqs. (5) and (6), is that the limited ability of single cells to sense high concentrations of chemoattractant, and the resulting limitation in their chemotactic response, can destabilize entire propagating fronts. To illustrate this, we recast our results in terms of the characteristic concentrations c_- and c_+ of the sensing function $f(c)$. Varying these concentrations tunes both $f'(c)$ and $f''(c)$, thus affecting the values of both $\alpha \equiv f'_0 c_\infty$ and $\beta \equiv -f''_0 c_\infty^2$, and hence changing the relative contribution of the stabilizing and the destabilizing mechanisms. Which effect wins when varying c_- and c_+ ?

For a given c_- , the front is unstable for values of c_+ close to c_- , i.e. for narrow sensing windows (darker curves in Fig. 2b). As c_+ increases, the destabilizing effect of the chemotactic response limitation becomes less important, and the front eventually becomes stable (lighter curves in Fig. 2b). Therefore, for a given c_- , the front switches from unstable to stable as the sensing window widens by increasing c_+ (Fig. 2c, corresponding to the purple dashed line in Fig. 2d). Conversely, the front can also be stabilized by narrowing the sensing window, e.g. by increasing c_- at fixed c_+ (moving up in Fig. 2d). Therefore, front stability is promoted by increasing the characteristic sensing concentrations c_- and c_+ . Although increasing c_- and c_+ weakens the chemotactic re-

sponse (Fig. 1b), it also makes the destabilizing response-limitation effects less pronounced. Finally, we recast the instability condition, Eq. (6), in terms of c_- and c_+ :

$$\frac{c_+}{c_\infty} < \frac{c_\infty}{c_-} \frac{2}{1 + 2\Gamma + \sqrt{1 + 4\Gamma}}. \quad (7)$$

The black dashed line in Fig. 2d shows the stability limit.

To test our predictions, we perform finite-element simulations of the full Eqs. (1) and (2) (SI). Introducing an initial perturbation with a long wavelength ($q\ell_d = 0.02$) and small amplitude ($A/\lambda = 0.016$), we find regimes of both front instability and stability (Fig. S1) in agreement with the stability diagram predicted analytically (Fig. S2).

Discussion. We have quantified the conditions for the stability of chemotactic fronts. Below the stability limit (Eq. (7)), we predict a morphological instability that could result in fingering patterns and even front disassembly. Expanding bacterial colonies form complex patterns that are thought to arise from bulk instabilities^{12,15,16,37,72,73}. However, the instability that we predict is fundamentally different, as it is interfacial and it arises purely from chemotaxis. To our knowledge, it has not been observed in experiments. Our predictions provide guidelines for future studies to search for it. For example, we predict front instability when the sensing concentrations c_- and c_+ are small compared to nutrient availability c_∞ (Fig. 2d). Therefore, experiments can probe this regime by either increasing nutrient availability or genetically impairing the cells' sensing ability. Moreover, we predict that fronts would destabilize over long wavelengths, at least of the order of the diffusion length ℓ_d (Fig. 2b). In experiments, fronts must therefore be sufficiently long to become unstable.

Front stability can have relevant biological implications. For example, in embryos, chemotactic cell groups must remain cohesive to develop into functional organs. In bacterial populations, cells must also stay together to collectively absorb sufficient chemoattractant to generate the chemical gradient driving front motion^{74,75}. Thus, inspired by our calculations, we speculate that the cells' sensing abilities might have evolved to avoid instability and ensure robust collective chemotaxis.

To probe this idea, we examine published experiments on chemotactic fronts of *E. coli*^{17,20}. These experiments report the concentrations c_- and c_+ for two different chemoattractants, as well as the parameters that determine the diffusio-absorption number Γ (Table II), with which we construct a stability diagram akin to Fig. 2d for each experiment (Fig. S4). The far-field concentrations c_∞ used in experiments likely represent upper bounds of those encountered in natural environments, and thus our estimates are in conditions most favorable for instability. Yet, we find that all experiments fall in the predicted *stable* regime. Consistently, the experiments observe stable flat fronts in all cases, suggesting that the ratios c_-/c_∞ and c_+/c_∞ are always high enough (Fig. S4). Further experiments are required to systematically test the tantalizing hypothesis that cellular sensing might be tuned to ensure stable collective chemotaxis.

Our results are also qualitatively consistent with recent experiments on 3D-printed bacterial populations, which

found that morphological perturbations are smoothed out by chemotaxis⁷⁶. These experiments, however, imposed large-amplitude perturbations in three-dimensional populations, whereas our analysis focuses on the small-amplitude limit in two dimensions. Hence, the experiments cannot be directly compared to our theory. Nevertheless, both demonstrate that sensing limitations of individual cells determine the stability of an entire chemotactic population.

Building on this finding, future work can explore how population morphology is affected by the chemotactic efficiency constraints imposed by biochemical^{77–80} and mechanical^{81,82} cell-cell interactions, switching between swimming states⁸³, and information acquisition requirements⁸⁴. Our work could also be generalized to account for collective sensing mechanisms⁷⁷ and for chemokinesis, i.e. the dependence of cell speed on chemical concentration⁸⁵. Furthermore, whereas the instability mechanisms that we identified arise from the deterministic dynamics of chemotaxis, future work can study the role of noise in selecting the resulting patterns. Beyond chemotaxis, our theory could be generalized to other types of collective tactic phenomena^{86–88} including cell durotaxis^{89,90}, electrotaxis⁹¹, and robot phototaxis^{92,93}. In these cases, as for chemotaxis, sensing increases and then saturates with the stimulus, be it substrate stiffness^{90,94},

electric field⁹¹, or light intensity^{92,93} — which, as quantified by the sensing function $f(c)$, is the essential feature of our theory. Specifically, in our analysis of chemotactic front propagation in terms of linear response theory, chemical gradients provide the driving force, and cellular sensing provides the response function. In these general terms, we conclude that, when modulated by a response function, the force that drives front propagation can also fully determine its stability.

Acknowledgments. We thank D.B. Amchin, T. Bhattacharjee, and N.S. Wingreen for useful discussions. R.A. acknowledges support from the Princeton Center for Theoretical Science, from the Human Frontier Science Program (LT000475/2018-C), and from the National Science Foundation through the Center for the Physics of Biological Function (PHY-1734030). A.M.-C. acknowledges support from the Princeton Center for Theoretical Science and the Human Frontier Science Program through the grant LT000035/2021-C. S.S.D. acknowledges support from NSF grant CBET-1941716, the Eric and Wendy Schmidt Transformative Technology Fund at Princeton, and the Princeton Center for Complex Materials, a Materials Research Science and Engineering Center supported by NSF grant DMR-2011750.

-
1. M. Cross and P. Hohenberg, “Pattern formation outside of equilibrium,” *Rev. Mod. Phys.* **65**, 851–1112 (1993).
 2. Michael Cross and Henry Greenside, *Pattern formation and dynamics in nonequilibrium systems* (Cambridge University Press, 2009).
 3. L. M. Pismen, *Patterns and interfaces in dissipative dynamics* (Springer, 2006).
 4. Rashmi C. Desai and Raymond Kapral, *Dynamics of self-organized and self-assembled structures* (Cambridge University Press, 2009).
 5. Wim van Saarloos, “Front propagation into unstable states,” *Phys. Rep.* **386**, 29–222 (2003).
 6. Pierre Colinet and Alexander Nepomnyashchy, eds., *Pattern Formation at Interfaces* (Springer, 2010).
 7. James Dickson Murray, *Mathematical Biology I. An Introduction*, 3rd ed. (Springer, 2002).
 8. Leah Edelstein-Keshet, *Mathematical Models in Biology* (Society for Industrial and Applied Mathematics, 2005).
 9. Jose Negrete and Andrew C. Oates, “Towards a physical understanding of developmental patterning,” *Nat. Rev. Genet.* **22**, 518–531 (2021).
 10. R.A. Fisher, “The wave of advance of advantageous genes,” *Ann. Eugen.* **7**, 355–369 (1937).
 11. A.N. Kolmogorov, I.G. Petrovsky, and N.S. Piskunov, “A study of the diffusion equation with increase in the amount of substance, and its application to a biological problem,” *Bull. Moscow Univ. Math. Mech.* **1**, 1–25 (1937).
 12. James Dickson Murray, *Mathematical Biology II. Spatial Models and Biomedical Applications*, 3rd ed. (Springer, 2003).
 13. Remy Colin, Bin Ni, Leonid Laganenka, and Victor Sourjik, “Multiple functions of flagellar motility and chemotaxis in bacterial physiology,” *FEMS Microbiol. Rev.* **45**, fuab038 (2021).
 14. J. Adler, “Chemotaxis in Bacteria,” *Science* **153**, 708–16 (1966).
 15. Elena O. Budrene and Howard C. Berg, “Complex patterns formed by motile cells of Escherichia coli,” *Nature* **349**, 630–633 (1991).
 16. Elena O. Budrene and Howard C. Berg, “Dynamics of formation of symmetrical patterns by chemotactic bacteria,” *Nature* **376**, 49–53 (1995).
 17. X. Fu, S. Kato, J. Long, H. H. Mattingly, C. He, D. C. Vural, S. W. Zucker, and T. Emonet, “Spatial self-organization resolves conflicts between individuality and collective migration,” *Nat. Commun.* **9**, 2177 (2018).
 18. Jonas Cremer, Tomoya Honda, Ying Tang, Jerome Wong-Ng, Massimo Vergassola, and Terence Hwa, “Chemotaxis as a navigation strategy to boost range expansion,” *Nature* **575**, 658–663 (2019).
 19. Sebastian Gude, Erçag Pinçé, Katja M. Taute, Anne-Bart Seinen, Thomas S. Shimizu, and Sander J. Tans, “Bacterial coexistence driven by motility and spatial competition,” *Nature* **578**, 588–592 (2020).
 20. Tapomoy Bhattacharjee, Daniel B Amchin, Jenna A Ott, Felix Kratz, and Sujit S Datta, “Chemotactic migration of bacteria in porous media,” *Biophys. J.* **120**, 3483–3497 (2021).
 21. Yang Bai, Caiyun He, Pan Chu, Junjia Long, Xuefei Li, and Xiongfei Fu, “Spatial modulation of individual behaviors enables an ordered structure of diverse phenotypes during bacterial group migration,” *eLife* **10**, e67316 (2021).
 22. Evelyn F. Keller and Lee A. Segel, “Initiation of slime mold aggregation viewed as an instability,” *J. Theor. Biol.* **26**, 399–415 (1970).
 23. Elena Scarpa and Roberto Mayor, “Collective cell migration in development,” *J. Cell Biol.* **212**, 143–55 (2016).
 24. K J Painter, P K Maini, and H G Othmer, “Stripe formation in juvenile Pomacanthus explained by a generalized Turing mechanism with chemotaxis,” *Proc. Natl. Acad. Sci. U. S. A.* **96**, 5549–

- 54 (1999).
25. Eric Theveneau, Lorena Marchant, Sei Kuriyama, Mazhar Gull, Barbara Moepps, Maddy Parsons, and Roberto Mayor, “Collective Chemotaxis Requires Contact-Dependent Cell Polarity,” *Dev. Cell* **19**, 39–53 (2010).
 26. Luke Tweedy, Peter A. Thomason, Peggy I. Paschke, Kirsty Martin, Laura M. Machesky, Michele Zagnoni, and Robert H. Insall, “Seeing around corners: Cells solve mazes and respond at a distance using attractant breakdown,” *Science* **369**, eaay9792 (2020).
 27. Gema Malet-Engra, Weimiao Yu, Amanda Oldani, Javier Rey-Barroso, Nir S Gov, Giorgio Scita, and Loïc Dupré, “Collective cell motility promotes chemotactic prowess and resistance to chemorepulsion,” *Curr. Biol.* **25**, 242–50 (2015).
 28. Alberto Puliafito, Alessandro De Simone, Giorgio Seano, Paolo Armando Gagliardi, Laura Di Blasio, Federica Chianale, Andrea Gamba, Luca Primo, and Antonio Celani, “Three-dimensional chemotaxis-driven aggregation of tumor cells,” *Sci. Rep.* **5**, 15205 (2015).
 29. Ah-Young Jee, Sandipan Dutta, Yoon-Kyoung Cho, Tsvi Tlusty, and Steve Granick, “Enzyme leaps fuel antichemotaxis,” *Proc. Natl. Acad. Sci. U. S. A.* **115**, 14–18 (2018).
 30. Jaime Agudo-Canalejo, Pierre Illien, and Ramin Golestanian, “Phoresis and Enhanced Diffusion Compete in Enzyme Chemotaxis,” *Nano Lett.* **18**, 2711–2717 (2018).
 31. Farzad Mohajerani, Xi Zhao, Ambika Somasundar, Darrell Velez-gol, and Ayusman Sen, “A Theory of Enzyme Chemotaxis: From Experiments to Modeling,” *Biochemistry* **57**, 6256–6263 (2018).
 32. Pierre Illien, Ramin Golestanian, and Ayusman Sen, “Fuelled motion: phoretic motility and collective behaviour of active colloids,” *Chem. Soc. Rev.* **46**, 5508–5518 (2017).
 33. Benno Liebchen and Hartmut Löwen, “Synthetic Chemotaxis and Collective Behavior in Active Matter,” *Acc. Chem. Res.* **51**, 2982–2990 (2018).
 34. Holger Stark, “Artificial Chemotaxis of Self-Phoretic Active Colloids: Collective Behavior,” *Acc. Chem. Res.* **51**, 2681–2688 (2018).
 35. Evelyn F. Keller and Lee A. Segel, “Model for chemotaxis,” *J. Theor. Biol.* **30**, 225–234 (1971).
 36. Evelyn F. Keller and Lee A. Segel, “Traveling bands of chemotactic bacteria: A theoretical analysis,” *J. Theor. Biol.* **30**, 235–248 (1971).
 37. M P Brenner, L S Levitov, and E O Budrene, “Physical mechanisms for chemotactic pattern formation by bacteria,” *Biophys. J.* **74**, 1677–93 (1998).
 38. Maximilian Seyrich, Andrzej Palugniok, and Holger Stark, “Traveling concentration pulses of bacteria in a generalized Keller–Segel model,” *New J. Phys.* **21**, 103001 (2019).
 39. Avaneesh V. Narla, Jonas Cremer, and Terence Hwa, “A traveling-wave solution for bacterial chemotaxis with growth,” *Proc. Natl. Acad. Sci. U. S. A.* **118**, e2105138118 (2021).
 40. J. P. Gollub and J. S. Langer, “Pattern formation in nonequilibrium physics,” *Rev. Mod. Phys.* **71**, S396–S403 (1999).
 41. R. Gonzalez-Cinca, R. Folch, R. Benitez, L. Ramirez-Piscina, J. Casademunt, and A. Hernandez-Machado, “Phase-field models in interfacial pattern formation out of equilibrium,” in *Adv. Condens. Matter Stat. Mech.*, edited by Elka Korutcheva and Rodolfo Cuerno (Nova Science Publishers, 2004) Chap. 9, pp. 203–236, arXiv:0305058 [cond-mat].
 42. Jaume Casademunt, “Viscous fingering as a paradigm of interfacial pattern formation: Recent results and new challenges,” *Chaos An Interdiscip. J. Nonlinear Sci.* **14**, 809–824 (2004).
 43. J. S. Langer, “Instabilities and pattern formation in crystal growth,” *Rev. Mod. Phys.* **52**, 1–28 (1980).
 44. Eshel Ben-Jacob and Peter Garik, “The formation of patterns in non-equilibrium growth,” *Nature* **343**, 523–530 (1990).
 45. P. G. Saffman and G. Taylor, “The penetration of a fluid into a porous medium or Hele-Shaw cell containing a more viscous liquid,” *Proc. R. Soc. A Math. Phys. Eng. Sci.* **245**, 312–329 (1958).
 46. W. W. Mullins and R. F. Sekerka, “Stability of a Planar Interface During Solidification of a Dilute Binary Alloy,” *J. Appl. Phys.* **35**, 444–451 (1964).
 47. Michelle Driscoll, Blaise Delmotte, Mena Youssef, Stefano Sacanna, Aleksandar Donev, and Paul Chaikin, “Unstable fronts and motile structures formed by microrollers,” *Nat. Phys.* **13**, 375–379 (2017).
 48. Evgeniy Khain and Leonard M. Sander, “Dynamics and Pattern Formation in Invasive Tumor Growth,” *Phys. Rev. Lett.* **96**, 188103 (2006).
 49. Michał Bogdan and Thierry Savin, “Fingering instabilities in tissue invasion: an active fluid model,” *R. Soc. Open Sci.* **5**, 181579 (2018).
 50. Eshel Ben-Jacob, Inon Cohen, and Herbert Levine, “Cooperative self-organization of microorganisms,” *Adv. Phys.* **49**, 395–554 (2000).
 51. Rosalind J Allen and Bartłomiej Waclaw, “Bacterial growth: a statistical physicist’s guide,” *Reports Prog. Phys.* **82**, 016601 (2019).
 52. Romain Mueller and Amin Doostmohammadi, “Phase field models of active matter,” (2021), arXiv:2102.05557.
 53. So Kitsunezaki, “Interface Dynamics for Bacterial Colony Formation,” *J. Phys. Soc. Japan* **66**, 1544–1550 (1997).
 54. Judith Müller and Wim van Saarloos, “Morphological instability and dynamics of fronts in bacterial growth models with nonlinear diffusion,” *Phys. Rev. E* **65**, 061111 (2002).
 55. F. D. C. Farrell, O. Hallatschek, D. Marenduzzo, and B. Waclaw, “Mechanically Driven Growth of Quasi-Two-Dimensional Microbial Colonies,” *Phys. Rev. Lett.* **111**, 168101 (2013).
 56. Amin Doostmohammadi, Sumesh P. Thampi, and Julia M. Yeomans, “Defect-Mediated Morphologies in Growing Cell Colonies,” *Phys. Rev. Lett.* **117**, 048102 (2016).
 57. Xin Wang, Howard A Stone, and Ramin Golestanian, “Shape of the growing front of biofilms,” *New J. Phys.* **19**, 125007 (2017).
 58. Sarah Trinschek, Karin John, and Uwe Thiele, “Modelling of surfactant-driven front instabilities in spreading bacterial colonies,” *Soft Matter* **14**, 4464–4476 (2018).
 59. Jing Yan, Chenyi Fei, Sheng Mao, Alexis Moreau, Ned S Wingreen, Andrej Košmrlj, Howard A Stone, and Bonnie L Bassler, “Mechanical instability and interfacial energy drive biofilm morphogenesis,” *eLife* **8**, e43920 (2019).
 60. Chenyi Fei, Sheng Mao, Jing Yan, Ricard Alert, Howard A Stone, Bonnie L Bassler, Ned S Wingreen, and Andrej Košmrlj, “Nonuniform growth and surface friction determine bacterial biofilm morphology on soft substrates,” *Proc. Natl. Acad. Sci. U. S. A.* **117**, 7622–7632 (2020).
 61. John J. Williamson and Guillaume Salbreux, “Stability and Roughness of Interfaces in Mechanically Regulated Tissues,” *Phys. Rev. Lett.* **121**, 238102 (2018).
 62. Tobias Büscher, Angel L Diez, Gerhard Gompper, and Jens Elgeti, “Instability and fingering of interfaces in growing tissue,” *New J. Phys.* **22**, 083005 (2020).
 63. Ricard Alert and Xavier Trepat, “Physical Models of Collective Cell Migration,” *Annu. Rev. Condens. Matter Phys.* **11**, 77–101 (2020).
 64. Carlos Pérez-González, Ricard Alert, Carles Blanch-Mercader, Manuel Gómez-González, Tomasz Kolodziej, Elsa Bazellieres, Jaume Casademunt, and Xavier Trepat, “Active wetting of ep-

- ithelial tissues," *Nat. Phys.* **15**, 79–88 (2019).
65. Ricard Alert, Carles Blanch-Mercader, and Jaume Casademunt, "Active Fingering Instability in Tissue Spreading," *Phys. Rev. Lett.* **122**, 088104 (2019).
 66. Carolina Trenado, Luis L. Bonilla, and Alejandro Martínez-Calvo, "Fingering instability in spreading epithelial monolayers: roles of cell polarisation, substrate friction and contractile stresses," *Soft Matter* **17**, 8276–8290 (2021).
 67. Eshel Ben-Jacob, Ofer Schochet, Adam Tenenbaum, Inon Cohen, Andras Czirók, and Tamas Vicsek, "Generic modelling of cooperative growth patterns in bacterial colonies," *Nature* **368**, 46–49 (1994).
 68. Martine Ben Amar, "Chemotaxis migration and morphogenesis of living colonies," *Eur. Phys. J. E* **36**, 64 (2013).
 69. M. Ben Amar, "Collective chemotaxis and segregation of active bacterial colonies," *Sci. Rep.* **6**, 21269 (2016).
 70. Mitsuo Funaki, Masayasu Mimura, and Tohru Tsujikawa, "Travelling front solutions arising in the chemotaxis-growth model," *Interfaces Free Boundaries* **8**, 223–245 (2006).
 71. Yevgeniy V Kalinin, Lili Jiang, Yuhai Tu, and Mingming Wu, "Logarithmic Sensing in Escherichia coli Bacterial Chemotaxis," *Biophys. J.* **96**, 2439–2448 (2009).
 72. M E Cates, D Marenduzzo, I Pagonabarraga, and J Tailleur, "Arrested phase separation in reproducing bacteria creates a generic route to pattern formation," *Proc. Natl. Acad. Sci. U. S. A.* **107**, 11715–11720 (2010).
 73. Michael P Brenner, "Chemotactic patterns without chemotaxis," *Proc. Natl. Acad. Sci. U. S. A.* **107**, 11653–4 (2010).
 74. Luke Tweedy, Olivia Susanto, and Robert H Insall, "Self-generated chemotactic gradients — cells steering themselves," *Curr. Opin. Cell Biol.* **42**, 46–51 (2016).
 75. Luke Tweedy and Robert H. Insall, "Self-Generated Gradients Yield Exceptionally Robust Steering Cues," *Front. Cell Dev. Biol.* **8**, 133 (2020).
 76. Tapomoy Bhattacharjee, Daniel B Amchin, Ricard Alert, Jenna Anne Ott, and Sujit Sankar Datta, "Chemotactic smoothing of collective migration," *eLife* **11**, e71226 (2022).
 77. Brian A Camley, "Collective gradient sensing and chemotaxis: modeling and recent developments," *J. Phys. Condens. Matter* **30**, 223001 (2018).
 78. David Ellison, Andrew Mugler, Matthew D Brennan, Sung Hoon Lee, Robert J Huebner, Eliah R Shamir, Laura A Woo, Joseph Kim, Patrick Amar, Ilya Nemenman, Andrew J Ewald, and Andre Levchenko, "Cell-cell communication enhances the capacity of cell ensembles to sense shallow gradients during morphogenesis," *Proc. Natl. Acad. Sci. U. S. A.* **113**, E679–688 (2016).
 79. Andrew Mugler, Andre Levchenko, and Ilya Nemenman, "Limits to the precision of gradient sensing with spatial communication and temporal integration," *Proc. Natl. Acad. Sci. U. S. A.* **113**, E689–695 (2016).
 80. Sean Fancher and Andrew Mugler, "Fundamental Limits to Collective Concentration Sensing in Cell Populations," *Phys. Rev. Lett.* **118**, 078101 (2017).
 81. Remy Colin, Knut Drescher, and Victor Sourjik, "Chemotactic behaviour of Escherichia coli at high cell density," *Nat. Commun.* **10**, 5329 (2019).
 82. Maojin Tian, Chi Zhang, Rongjing Zhang, and Junhua Yuan, "Collective motion enhances chemotaxis in a two-dimensional bacterial swarm," *Biophys. J.* **120**, 1615–1624 (2021).
 83. Zahra Alirezaeianjani, Robert Großmann, Veronika Pfeifer, Marius Hintsche, and Carsten Beta, "Chemotaxis strategies of bacteria with multiple run modes," *Sci. Adv.* **6**, eaaz6153 (2020).
 84. H H Mattingly, K Kamino, B B Machta, and T Emonet, "Escherichia coli chemotaxis is information limited," *Nat. Phys.* **17**, 1426–1431 (2021).
 85. Theresa Jakuszeit, James Lindsey-Jones, François J. Peaudecerf, and Ottavio A. Croze, "Migration and accumulation of bacteria with chemotaxis and chemokinesis," *Eur. Phys. J. E* **44**, 32 (2021).
 86. Pere Roca-Cusachs, Raimon Sunyer, and Xavier Trepat, "Mechanical guidance of cell migration: Lessons from chemotaxis," *Curr. Opin. Cell Biol.* **25**, 543–549 (2013).
 87. Adam Shellard and Roberto Mayor, "All Roads Lead to Directional Cell Migration," *Trends Cell Biol.* **30**, 852–868 (2020).
 88. Shuvasree SenGupta, Carole A. Parent, and James E. Bear, "The principles of directed cell migration," *Nat. Rev. Mol. Cell Biol.* **22**, 529–547 (2021).
 89. Raimon Sunyer, Vito Conte, Jorge Escribano, Alberto Elosegui-Artola, Anna Labernadie, Léo Valon, Daniel Navajas, José Manuel García-Aznar, José J. Muñoz, Pere Roca-Cusachs, and Xavier Trepat, "Collective cell durotaxis emerges from long-range intercellular force transmission," *Science* **353**, 1157–1161 (2016).
 90. Ricard Alert and Jaume Casademunt, "Role of Substrate Stiffness in Tissue Spreading: Wetting Transition and Tissue Durotaxis," *Langmuir* **35**, 7571–7577 (2019).
 91. Daniel J Cohen, W James Nelson, and Michel M Maharbiz, "Galvanotactic control of collective cell migration in epithelial monolayers," *Nat. Mater.* **13**, 409–417 (2014).
 92. Mite Mijalkov, Austin McDaniel, Jan Wehr, and Giovanni Volpe, "Engineering Sensorial Delay to Control Phototaxis and Emergent Collective Behaviors," *Phys. Rev. X* **6**, 011008 (2016).
 93. Stefano Palagi and Peer Fischer, "Bioinspired microrobots," *Nat. Rev. Mater.* **3**, 113–124 (2018).
 94. Marion Ghibaudo, Alexandre Saez, Léa Trichet, Alain Xayaphoummine, Julien Browaeys, Pascal Silberzan, Axel Buguin, and Benoît Ladoux, "Traction forces and rigidity sensing regulate cell functions," *Soft Matter* **4**, 1836–1843 (2008).

Supplementary Material for “Cellular Sensing Governs the Stability of Chemotactic Fronts”

Ricard Alert, Alejandro Martínez-Calvo, and Sujit S. Datta

I. THE STEP-PROFILE APPROXIMATION

The step-profile approximation (Fig. 1c, green) is based on two assumptions:

- (a) the cell concentration remains uniform inside the pulse ($s < 0$), and
- (b) the cell concentration drops suddenly to zero ahead of the pulse ($s > 0$).

Assumption (a) is often fulfilled in experiments. For example, for the experiments of Ref.²⁰ (parameter values in Table I), the cell pulse is about 700 μm wide whereas the chemoattractant penetrates only about $\ell_i \approx 7 \mu\text{m}$ into the pulse. The pulse can therefore be approximated as infinitely wide, with an approximately uniform cell concentration across the region where the chemoattractant concentration varies. More generally, from the classic work of Keller and Segel in Ref.³⁵, the pulse width is of the order of $w \sim D_\rho/v_0$. Assumption (a) then holds as long as $w/\ell_i \gg 1$. Using the definition of ℓ_i as listed in Table I, this condition amounts to $D_\rho/v_0 \times \sqrt{k\rho_p/(D_c c_M)} \gg 1$. Therefore, assumption a is a controlled approximation.

In contrast, assumption (b) is uncontrolled. We thus test its validity in numerical solutions of the full Eqs. (1) and (2), as described in Section III. We find that, from the initial condition, the decay of cell concentration ahead of the front becomes even sharper when the front is transversely unstable, and it smoothes out when the front is stable Fig. S3. Therefore, the step-profile approximation is particularly applicable to conditions of front instability.

Overall, the step-profile approximation allows us to make analytical progress and thereby identify the physical mechanisms of front stability. The competing mechanisms that we identify, i.e. the gradient and the response mechanisms, are general conclusions that hold irrespective of the accuracy of our calculation.

II. LINEAR STABILITY ANALYSIS

Here, we provide the details of the linear stability analysis of chemotactic fronts. As explained in the Main Text, we impose a perturbation $\delta x_f(y, t)$ on the front position, corresponding to a traveling cell density field $\rho(x, y, t) = \rho_0(s - \delta x_f(y, t))$, which has the same step profile as for the unperturbed front. As a result of the front perturbations, the chemoattractant field will be $c(x, y, t) = c_0(s) + \delta c(s, y, t)$, whose perturbation will rapidly reach a quasi-stationary traveling profile $\delta c(s, y)$ that follows the slowly-evolving cell front.

Chemoattractant perturbations. As for the unperturbed chemoattractant profile in Eq. (3), we determine $\delta c(s, y)$ sep-

arately in the regions ahead and inside the cell pulse. Ahead of the pulse, there is no chemoattractant absorption, and hence Eq. (1) reduces to

$$\partial_t c^a = D_c \nabla^2 c^a. \quad (\text{S1})$$

Respectively, inside the pulse, cell concentration is uniform, $\rho = \rho_p$. Approximating the chemoattractant uptake function by $g(c) \approx c/c_M$ as explained in the Main Text, Eq. (1) inside the pulse reduces to

$$\partial_t c^i = D_c \nabla^2 c^i - \frac{k\rho_p}{c_M} c^i, \quad (\text{S2})$$

Assuming a propagating solution $c(x, y, t) = c(x - v_0 t, y)$, linearizing Eqs. (S1) and (S2), and expressing them in terms of the comoving coordinate $s = x - v_0 t$, we obtain

$$-v_0 \partial_s \delta c^a(s, y) = D_c (\partial_s^2 + \partial_y^2) \delta c^a(s, y), \quad (\text{S3a})$$

$$-v_0 \partial_s \delta c^i(s, y) = D_c (\partial_s^2 + \partial_y^2) \delta c^i(s, y) - \frac{k\rho_p}{c_M} \delta c^i(s, y). \quad (\text{S3b})$$

To solve these equations, we decompose $\delta c(s, y)$ in Fourier modes along the \hat{y} axis:

$$\delta c(s, y) = \int_{-\infty}^{\infty} \delta \tilde{c}(s, q) e^{iqy} \frac{dq}{2\pi}. \quad (\text{S4})$$

In Fourier components, Eq. (S3) becomes

$$-v_0 \partial_s \delta \tilde{c}^a = D_c (\partial_s^2 - q^2) \delta \tilde{c}^a, \quad (\text{S5a})$$

$$-v_0 \partial_s \delta \tilde{c}^i = D_c (\partial_s^2 - q^2) \delta \tilde{c}^i - \frac{k\rho_p}{c_M} \delta \tilde{c}^i. \quad (\text{S5b})$$

The propagating solutions to these equations are

$$\delta \tilde{c}^a(s, q) = C_a \exp \left[-\frac{s}{2\ell_d} \left(1 + \sqrt{1 + 4q^2 \ell_d^2} \right) \right], \quad (\text{S6a})$$

$$\delta \tilde{c}^i(s, q) = C_i \exp \left[\frac{s}{2\ell_d} \left(\sqrt{1 + 4(\Gamma + q^2 \ell_d^2)} - 1 \right) \right]. \quad (\text{S6b})$$

Here, as explained in the Main Text, we have defined $\ell_d \equiv D_c/v_0$ and $\Gamma \equiv \ell_d/\ell_a$, with $\ell_a \equiv v_0 c_M/(k\rho_p)$. Moreover, we have already set two integration constants by imposing $\delta c^a(s \rightarrow \infty, y) = 0$ and $\delta c^i(s \rightarrow -\infty, y) = 0$. The remaining two integration constants, C_a and C_i , are determined by imposing equality of both chemoattractant concentration and diffusive flux at the perturbed front: $c^a(\delta x_f(y), y) = c^i(\delta x_f(y), y)$ and $\partial_s c^a(\delta x_f(y), y) = \partial_s c^i(\delta x_f(y), y)$. Expanding these conditions to first order in perturbations, we obtain

$$\delta c^a(0) = \delta c^i(0), \quad (\text{S7a})$$

$$\partial_s \delta c^a(0) + \partial_s^2 c_0^a(0) \delta x_f = \partial_s \delta c^i(0) + \partial_s^2 c_0^i(0) \delta x_f, \quad (\text{S7b})$$

which give

$$C_a = C_i = -c_\infty \frac{\sqrt{1+4\Gamma} - 1}{\sqrt{1+4q^2\ell_d^2} + \sqrt{1+4(\Gamma+q^2\ell_d^2)}} \frac{\delta\tilde{x}_f}{\ell_d}. \quad (\text{S8})$$

For $\Gamma \gg 1$ as in our parameter estimates (Table I), the chemoattractant perturbation profile can be approximated as

$$\delta\tilde{c}^a(s, q) \approx C_a \exp \left[-\frac{s}{2\ell_d} \left(1 + \sqrt{1+4q^2\ell_d^2} \right) \right], \quad (\text{S9a})$$

$$\delta\tilde{c}^i(s, q) \approx C_i \exp \left[\frac{s}{\ell_d} \sqrt{\Gamma + q^2\ell_d^2} \right], \quad (\text{S9b})$$

with

$$C_a \approx -c_\infty \frac{2\sqrt{\Gamma}}{\sqrt{1+4q^2\ell_d^2} + 2\sqrt{\Gamma+q^2\ell_d^2}} \frac{\delta\tilde{x}_f}{\ell_d}. \quad (\text{S10})$$

Interpretation. To interpret these results, let's consider a sinusoidal front perturbation of amplitude δA and wavenumber k : $\delta x_f(y) = \delta A \sin(ky)$. For this perturbation, we obtain $\delta\tilde{x}_f(q)$, introduce it in Eq. (S6) via Eq. (S8), and perform an inverse Fourier transform to obtain the chemoattractant perturbations in real space:

$$\begin{aligned} \delta c^a(s, y) &= -C \exp \left[-\frac{s}{2\ell_d} \left(1 + \sqrt{1+4k^2\ell_d^2} \right) \right] \\ &\quad \times \frac{\delta A}{\ell_d} \sin(ky), \end{aligned} \quad (\text{S11a})$$

$$\begin{aligned} \delta c^i(s, y) &= -C \exp \left[\frac{s}{2\ell_d} \left(\sqrt{1+4(\Gamma+k^2\ell_d^2)} - 1 \right) \right] \\ &\quad \times \frac{\delta A}{\ell_d} \sin(ky), \end{aligned} \quad (\text{S11b})$$

where

$$C = c_\infty \frac{\sqrt{1+4\Gamma} - 1}{\sqrt{1+4k^2\ell_d^2} + \sqrt{1+4(\Gamma+k^2\ell_d^2)}} \quad (\text{S12})$$

is a positive constant. These results show that in regions around peaks (Fig. 1a), where the front protrudes outward ($\sin(ky) > 0$), chemoattractant becomes absorbed, and its concentration decreases ($\delta c < 0$). Conversely, in regions around valleys (Fig. 1a), where the front bends inward ($\sin(ky) < 0$), chemoattractant becomes replenished and its concentration increases ($\delta c > 0$). Hence, in protruding regions, the chemoattractant gradient is increased ahead of the front ($s > 0$) but decreased inside the front ($s < 0$); compare peak and flat in Fig. 1c. Respectively, in intruding regions, the chemoattractant gradient is decreased ahead of the front ($s > 0$) but increased inside the front ($s < 0$); compare valley and flat in Fig. 1c.

Growth rate of front perturbations. Front perturbations evolve at a rate given by the perturbation in front speed $\delta v(y, t) = \partial_t \delta x_f(y, t)$. To obtain δv , we linearize the cell

concentration dynamics Eq. (2). For the imposed traveling solution $\rho(x, y, t) = \rho_0(s - \delta x_f(y, t))$, and in terms of the comoving coordinate $s = x - v_0 t$, we obtain:

$$\begin{aligned} -\delta v \partial_s \rho_0 &= -\partial_s (\rho_0 \chi [f'(c_0) \partial_s \delta c + f''(c_0) \partial_s c_0 \delta c]) \\ &\quad - \rho_0 \chi f'(c_0) \partial_y^2 \delta c - D_\rho \partial_s \rho_0 \partial_y^2 \delta x_f. \end{aligned} \quad (\text{S13})$$

The left-hand-side term is the advective flux due to perturbations in front motion. The right-hand-side term on the first line, with the ∂_s derivative, results from chemotactic fluxes in the propagation direction (\hat{x}). Respectively, the terms on the second line correspond to fluxes in the transverse direction (\hat{y}), which stem from both directed (chemotactic, χ) and undirected (diffusive, D_ρ) cell motion.

To solve for δv , we integrate Eq. (S13) over s , taking into account that ρ_0 corresponds to a step profile, and keeping terms only to first order in perturbations. We then transform to Fourier space and obtain

$$\begin{aligned} \delta\tilde{v} &= \chi \left[f'_0 \partial_s \delta\tilde{c}(0, q) + f''_0 \partial_s c_0(0) \delta\tilde{c}(0, q) \right. \\ &\quad \left. - q^2 \int_{-\infty}^0 f'(c_0(s)) \delta\tilde{c}(s, q) ds \right] - D_\rho q^2 \delta\tilde{x}_f, \end{aligned} \quad (\text{S14})$$

where $f'_0 \equiv f'(c_0(0)) > 0$, $f''_0 \equiv f''(c_0(0)) < 0$ are the slope and curvature of the sensing function $f(c)$ at the unperturbed front ($s = 0$). To complete the calculation of $\delta\tilde{v}$, we introduce our previous result for the chemoattractant perturbations $\delta\tilde{c}(s, q)$ (Eq. (S6)). Note that the chemoattractant gradient perturbation must be evaluated inside the pulse, where there are cells, as opposed to cell-free region ahead of the front. Therefore, $\partial_s \delta\tilde{c}(0, q) = \lim_{s \rightarrow 0^-} \partial_s \delta\tilde{c}(s, q)$, which we evaluate using Eq. (S6b). For the same reason, the integral in Eq. (S14) runs only up to $s = 0$.

Finally, to obtain the growth rate $\omega(q)$ of front perturbation modes, we use that $\delta v(y, t) = \partial_t \delta x_f(y, t)$. In Fourier space, we have $\delta\tilde{v}(q) = \omega(q) \delta\tilde{x}_f(q)$, and therefore the growth rate is $\omega(q) = \delta\tilde{v}(q) / \delta\tilde{x}_f(q)$. To obtain a closed analytical expression for the growth rate, we approximate the integral in Eq. (S14) by $f'_0 \int_{-\infty}^0 \delta\tilde{c}(s, q) ds$, which overestimates the contribution of the transverse chemotactic flux. Then, introducing the chemoattractant perturbations Eq. (S6) with Eq. (S8), we obtain

$$\begin{aligned} \omega(q) &= -D_\rho q^2 + \frac{\chi}{\ell_d^2} \frac{\sqrt{1+4\Gamma} - 1}{\sqrt{1+4q^2\ell_d^2} + \sqrt{1+4(\Gamma+q^2\ell_d^2)}} \\ &\quad \times \left[\beta \frac{\sqrt{1+4\Gamma} - 1}{\sqrt{1+4\Gamma} + 1} - \frac{\alpha}{2} \left(\sqrt{1+4(\Gamma+q^2\ell_d^2)} - 1 \right) \right. \\ &\quad \left. - 2\alpha \frac{q^2\ell_d^2}{\sqrt{1+4(\Gamma+q^2\ell_d^2)} - 1} \right], \end{aligned} \quad (\text{S15})$$

which we quote in Eq. (5) in the Main Text. Here, we have expressed f'_0 and f''_0 in terms of their corresponding positive dimensionless numbers $\alpha = f'_0 c_\infty$ and $\beta = -f''_0 c_\infty^2$, as explained in the Main Text. In the long-wavelength limit $q \rightarrow 0$,

the growth rate tends to

$$\omega(0) = \frac{\chi}{\ell_d^2} \left(\frac{\sqrt{1+4\Gamma}-1}{\sqrt{1+4\Gamma}+1} \right)^2 \left[\beta - \frac{\alpha}{2} \left(\sqrt{1+4\Gamma} + 1 \right) \right], \quad (\text{S16})$$

as we quote and discuss in the Main Text. Finally, in the limit $\Gamma \gg 1$ corresponding to our parameter estimates (Table I), these results are approximated as

$$\begin{aligned} \omega(q) \approx -D_\rho q^2 + \frac{\chi}{\ell_d^2} \frac{2\sqrt{\Gamma}}{\sqrt{1+4q^2\ell_d^2} + 2\sqrt{\Gamma+q^2\ell_d^2}} \\ \times \left[\beta - \alpha \sqrt{\Gamma+q^2\ell_d^2} - \alpha \frac{q^2\ell_d^2}{\sqrt{\Gamma+q^2\ell_d^2}} \right], \end{aligned} \quad (\text{S17})$$

and

$$\omega(0) \approx \frac{\chi}{\ell_d^2} \left[\beta - \alpha \sqrt{\Gamma} \right]. \quad (\text{S18})$$

III. NUMERICAL SIMULATIONS

We perform two-dimensional (2D) numerical simulations of the full Eqs. (1) and (2), only with the approximation $g(c) \approx c/c_M$ as discussed in the Main Text. To this end, we make the equations dimensionless using the characteristic scales deduced in the Main Text, which define the following dimensionless variables for the position vector, time, and the cell density and chemoattractant concentration fields:

$$\tilde{r} = \frac{\mathbf{r}}{\ell_d} = \frac{\mathbf{r}v_0}{D_c}, \quad \tilde{t} = \frac{t}{\tau} = \frac{t\chi}{\ell_d^2}, \quad \tilde{c} = \frac{c}{c_\infty}, \quad \tilde{\rho} = \frac{\rho}{\rho_p}. \quad (\text{S19})$$

In these dimensionless variables, Eqs. (1) and (2) read

$$\partial_{\tilde{t}} \tilde{c} = \frac{D_c}{\chi} [\nabla^2 \tilde{c} - \Gamma \tilde{\rho} \tilde{c}], \quad \text{in } \mathcal{V}, \quad (\text{S20a})$$

$$\partial_{\tilde{t}} \tilde{\rho} = \frac{D_\rho}{\chi} \nabla^2 \tilde{\rho} - \nabla \cdot [\tilde{\rho} \nabla f(\tilde{c})], \quad \text{in } \mathcal{V}, \quad (\text{S20b})$$

where $\mathcal{V} = (0, \tilde{L}_x) \times (0, \tilde{L}_y)$ is the 2D domain, $f(\tilde{c}) = \ln \left[\frac{1+\tilde{c}/(c_-/c_\infty)}{1+\tilde{c}/(c_+/c_\infty)} \right]$ is the sensing function, and $\Gamma = \ell_d/\ell_a = D_c k \rho_p / (v_0^2 c_M)$ is the diffusio-absorption number defined in the Main Text. We impose the following boundary conditions:

$$\tilde{c} = 0, \quad \text{and} \quad \hat{x} \cdot \nabla \tilde{\rho} = 0, \quad \text{at } \tilde{x} = 0 \quad (\text{S21a})$$

$$\tilde{c} = 1, \quad \text{and} \quad \hat{x} \cdot \nabla \tilde{\rho} = 0, \quad \text{at } \tilde{x} = \tilde{L}_x \quad (\text{S21b})$$

$$\hat{y} \cdot \nabla \tilde{c} = 0 \quad \text{and} \quad \hat{y} \cdot \nabla \tilde{\rho} = 0 \quad \text{at } \tilde{y} = 0, \tilde{L}_y, \quad (\text{S21c})$$

where \hat{x} and \hat{y} are the Cartesian unitary vectors.

As an initial condition, we impose a cell density profile with a perturbation of dimensionless wavevector $\tilde{q} = 4\pi/\tilde{L}_y$ and amplitude \tilde{A} :

$$\tilde{\rho}(\tilde{\mathbf{r}}, \tilde{t}=0) = \frac{1}{2} \left(1 - \tanh \left[\frac{\tilde{x} - 1 + \tilde{A} \cos(\tilde{q}\tilde{y})}{\tilde{\delta}} \right] \right), \quad (\text{S22})$$

where $\tilde{\delta} = 3$ sets the initial front width in the dimensionless simulation units. The initial chemoattractant concentration is determined by solving Eq. (S20b) with the boundary conditions in Eq. (S21).

We carry out numerical simulations using the finite-element method, which involves writing the equations in weak form by means of the integral scalar product using test functions $\tilde{\varphi}_\rho$ and $\tilde{\varphi}_c$ for the cell density $\tilde{\rho}(\tilde{\mathbf{r}}, \tilde{t})$ and chemoattractant concentration $\tilde{c}(\tilde{\mathbf{r}}, \tilde{t})$ fields, respectively. Using Green identities, we obtain an integral bilinear system of equations for the variables and their test functions:

$$\begin{aligned} \int_{\mathcal{V}} d\mathcal{V} \partial_{\tilde{t}} \tilde{c} \tilde{\varphi}_c + \frac{D_c}{\chi} \int_{\mathcal{V}} d\mathcal{V} \nabla \tilde{c} \cdot \nabla \tilde{\varphi}_c \\ - \frac{D_c}{\chi} \int_{\mathcal{C}} d\mathcal{C} \nabla \tilde{c} \cdot \mathbf{n} \tilde{\varphi}_c + \frac{D_c}{\chi} \Gamma \int_{\mathcal{V}} d\mathcal{V} \tilde{c} \tilde{\rho} \tilde{\varphi}_c = 0, \end{aligned} \quad (\text{S23a})$$

$$\begin{aligned} \int_{\mathcal{V}} d\mathcal{V} \partial_{\tilde{t}} \tilde{\rho} \tilde{\varphi}_\rho + \int_{\mathcal{V}} d\mathcal{V} \left[\frac{D_\rho}{\chi} \nabla \tilde{\rho} - \tilde{\rho} \nabla f(\tilde{c}) \right] \cdot \nabla \tilde{\varphi}_\rho \\ - \int_{\mathcal{C}} d\mathcal{C} \left[\frac{D_\rho}{\chi} \nabla \tilde{\rho} - \tilde{\rho} \nabla f(\tilde{c}) \right] \cdot \mathbf{n} \tilde{\varphi}_\rho = 0. \end{aligned} \quad (\text{S23b})$$

Here, \mathbf{n} is the outer unit normal of the boundaries \mathcal{C} of the 2D domain \mathcal{V} , and $d\mathcal{V}$ and $d\mathcal{C}$ are the surface and line elements, respectively. To ensure numerical stability, the equations are discretized in space using second-order Lagrange polynomials and triangular elements for the fields, and evolved in time through a 4th-order variable-step backward differentiation formula method. The relative tolerance of the nonlinear method is always set below 10^{-6} . The time-dependent solver was complemented with an automatic refining mesh algorithm which increased the number of mesh elements depending on the absolute value of the cell density gradient at the traveling front.

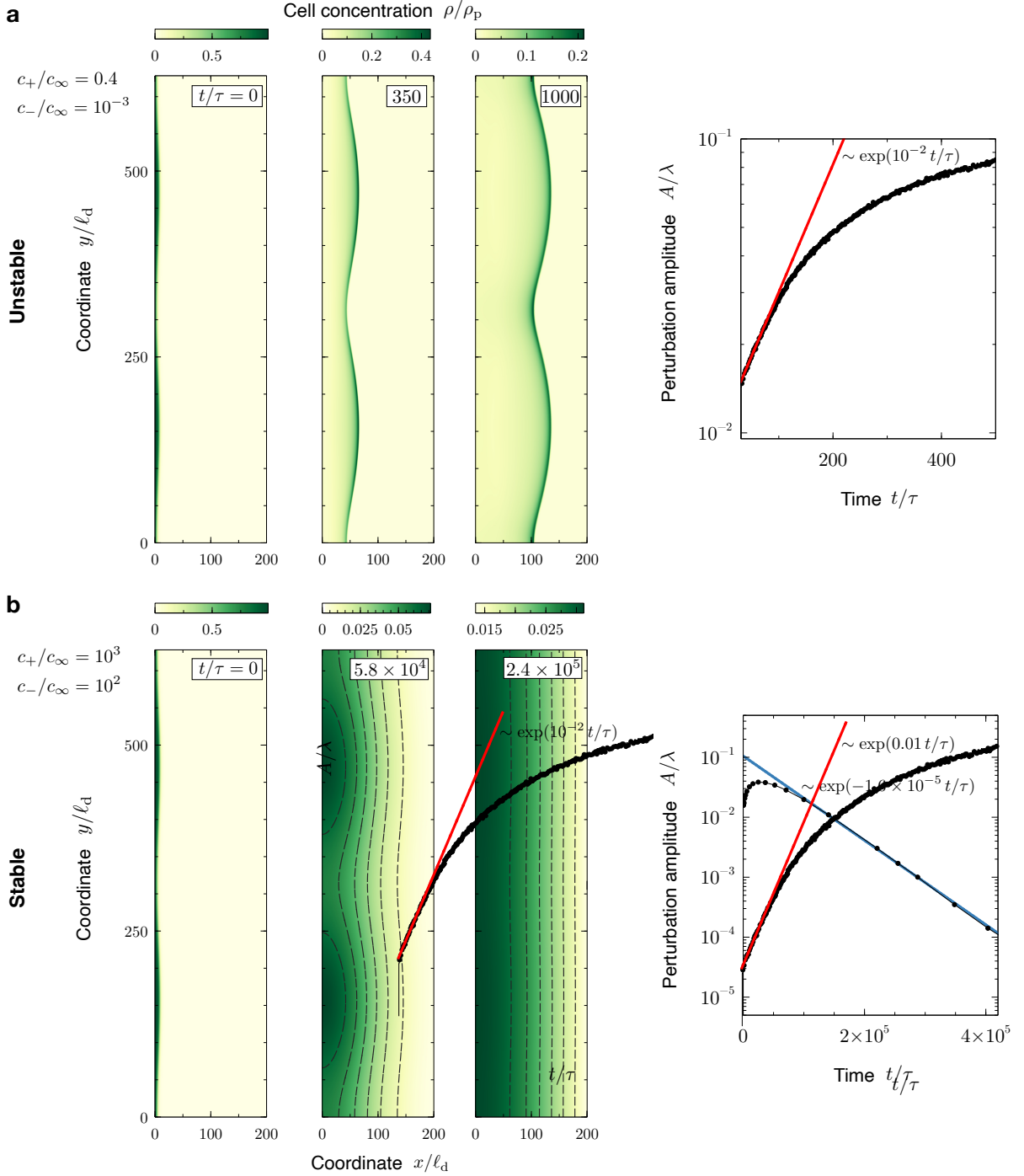


Figure S1 | Numerical simulations of stable and unstable chemotactic fronts. Snapshots of propagating cell pulses in the unstable (a) and stable (b) regimes. In the stable case, dashed lines indicate isocontours of the cell concentration field. The cell pulse is initially perturbed as given by Eq. (S22) with a wavenumber $q\ell_d = 0.02$ and amplitude $A/\lambda = 0.016$, where $\lambda = 2\pi/q$. The right panels show the growth and decay of the perturbation amplitude over time for the unstable and stable cases, respectively. Red and blue lines are exponential fits that characterize the linear regime of the unstable and stable dynamics, respectively. The corresponding growth and decay rates are shown in the plots. Parameter values are $\Gamma = 11$, $D_\rho/\chi = 0.05$, and $D_c/\chi = 0.01$, and the unstable and stable regimes are obtained by choosing different values for the sensing concentrations c_- and c_+ as indicated in the plot.

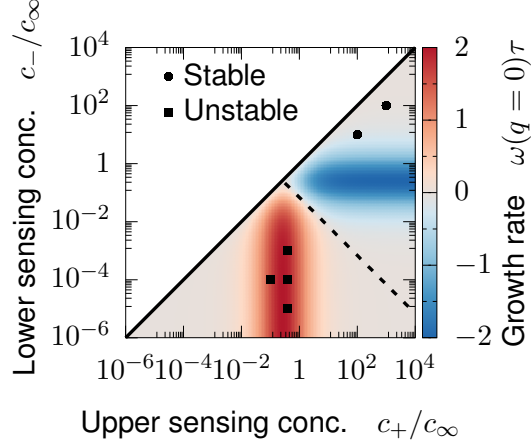


Figure S2 | Simulation results (points) agree with the stability diagram predicted analytically. The dashed line indicates the stability limit given by Eq. (7). Simulations with values of c_- and c_+ falling within the stable and unstable regime indeed show stable and unstable front dynamics, respectively. Parameter values other than c_- and c_+ are given in Fig. S1.

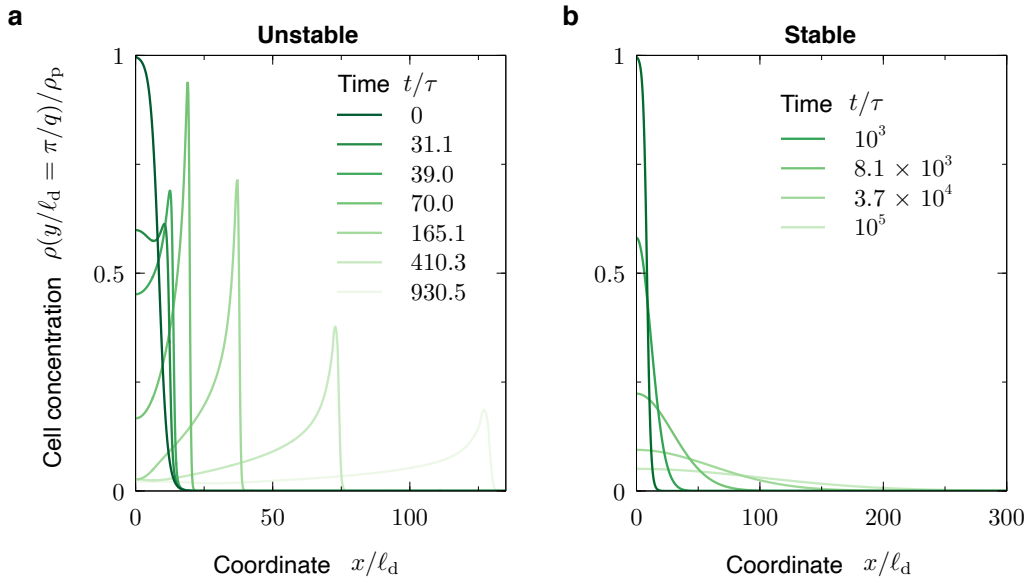


Figure S3 | Cell concentration profiles in numerical simulations. The cell concentration profile develops a sharper front in the unstable regime (a) than in the stable one (b). Parameter values for each case are as given in Fig. S1.

Description	Estimate
Chemoattractant diffusivity	$D_c \sim 800 \mu\text{m}^2/\text{s}$
Maximal absorption rate per cell	$k \sim 2 \times 10^6 \text{ s}^{-1}$
Half-maximum absorption concentr.	$c_M \sim 1 \mu\text{M}$
Far-field chemoattractant concentr.	$c_\infty \sim 10 \text{ mM}$
Upper sensing concentration	$c_+ \sim 30 \mu\text{M}$
Lower sensing concentration	$c_- \sim 1 \mu\text{M}$
Effective cell diffusivity	$D_\rho \sim 0.9 \mu\text{m}^2/\text{s}$
Chemotactic susceptibility	$\chi \sim 9 \mu\text{m}^2/\text{s}$
Cell concentration in the front	$\rho_f \sim 0.0048 \mu\text{m}^{-3}$
Front speed	$v_0 \sim 0.042 \mu\text{m/s}$
Diffusion length	$\ell_d = D_c/v_0 \sim 19 \text{ mm}$
Absorption length	$\ell_a = v_0 c_M / (k \rho_f) \sim 2.7 \text{ nm}$
Internal decay length	$\ell_i = \sqrt{\ell_d \ell_a} \sim 7 \mu\text{m}$
Diffusio-absorption number	$\Gamma = \ell_d/\ell_a \sim 7.2 \times 10^6$
Chemotactic response number	$\alpha = f'_0 c_\infty \sim 1.8 \times 10^3$
Response limitation number	$\beta = f''_0 c_\infty^2 \sim 4.4 \times 10^6$

Table I | Estimates of model parameters. The values correspond to *E. coli* cells migrating toward the amino acid serine through porous media, as in Ref.²⁰. The first and second parts of the table correspond to parameters related to chemoattractant and cell motion, respectively. The third part corresponds to parameters derived here from the above. To obtain α and β , we evaluate $f'_0 = f'(c_0(0))$ and $f''_0 = f''(c_0(0))$ using Eq. (3) to calculate $c_0(0)$.

Parameter	Experiment					
	<i>E. coli</i> and aspartate, Fu et al. ¹⁷			<i>E. coli</i> and serine, Bhattacharjee et al. ²⁰		
	$c_\infty = 50 \mu\text{M}$	$c_\infty = 100 \mu\text{M}$	$c_\infty = 200 \mu\text{M}$	$\xi = 1.2 \mu\text{m}$	$\xi = 1.7 \mu\text{m}$	$\xi = 2.2 \mu\text{m}$
Chemoattractant diffusivity $D_c (\mu\text{m}^2/\text{s})$	500	500	500	800	800	800
Maximal absorption rate per cell $k (\text{s}^{-1})$	9.3×10^4	9.3×10^4	9.3×10^4	9.6×10^6	9.6×10^6	9.6×10^6
Half-maximum absorption concentr. $c_M (\mu\text{M})$	0.5	0.5	0.5	1	1	1
Far-field chemoattractant concentr. $c_\infty (\mu\text{M})$	50	100	200	10^4	10^4	10^4
Upper sensing concentration $c_+ (\mu\text{M})$	10^3	10^3	10^3	30	30	30
Lower sensing concentration $c_- (\mu\text{M})$	3.5	3.5	3.5	1	1	1
Effective cell diffusivity $D_\rho (\mu\text{m}^2/\text{s})$	165	165	165	0.4	0.9	2.3
Chemotactic susceptibility $\chi (\mu\text{m}^2/\text{s})$	3.6×10^3	3.6×10^3	3.6×10^3	5	9	145
Cell concentration in the pulse $\rho_p (\mu\text{m}^{-3})$	0.0015	0.0038	0.010	0.014	0.0048	0.048
Front speed $v_0 (\mu\text{m/s})$	5.0	3.4	3.2	0.017	0.042	0.25
Diffusion length $\ell_d = D_c/v_0 (\text{mm})$	0.10	0.15	0.16	47	19	3.2
Absorption length $\ell_a = v_0 c_M / (k \rho_p) (\mu\text{m})$	13	3.4	1.1	7.6×10^{-5}	5.5×10^{-4}	3.3×10^{-4}
Internal decay length $\ell_i = \sqrt{\ell_d \ell_a} (\mu\text{m})$	36	23	13	1.9	3.2	1.0
Diffusio-absorption number $\Gamma = \ell_d/\ell_a$	11	57	161	6.2×10^8	3.5×10^7	9.8×10^6
Chemotactic response number $\alpha = f'_0 c_\infty$	2.8	5.9	10	6.8×10^3	3.4×10^3	2.1×10^3
Response limitation number $\beta = f''_0 c_\infty^2$	8.2	36	110	5.1×10^7	1.4×10^7	5.6×10^6

Table II | Estimates of parameter values for experiments of bacterial chemotactic fronts. In the experiments by Fu et al.¹⁷, bacteria swim in liquid media with three different initial chemoattractant concentrations c_∞ . In the experiments by Bhattacharjee et al.²⁰, bacteria swim through porous media of three different pore sizes ξ . As in Table I, the first and second parts of the table correspond to parameters related to chemoattractant and cell motion, respectively. The third part corresponds to parameters derived here from the above. To obtain α and β , we evaluate $f'_0 = f'(c_0(0))$ and $f''_0 = f''(c_0(0))$ using Eq. (3) to calculate $c_0(0)$.

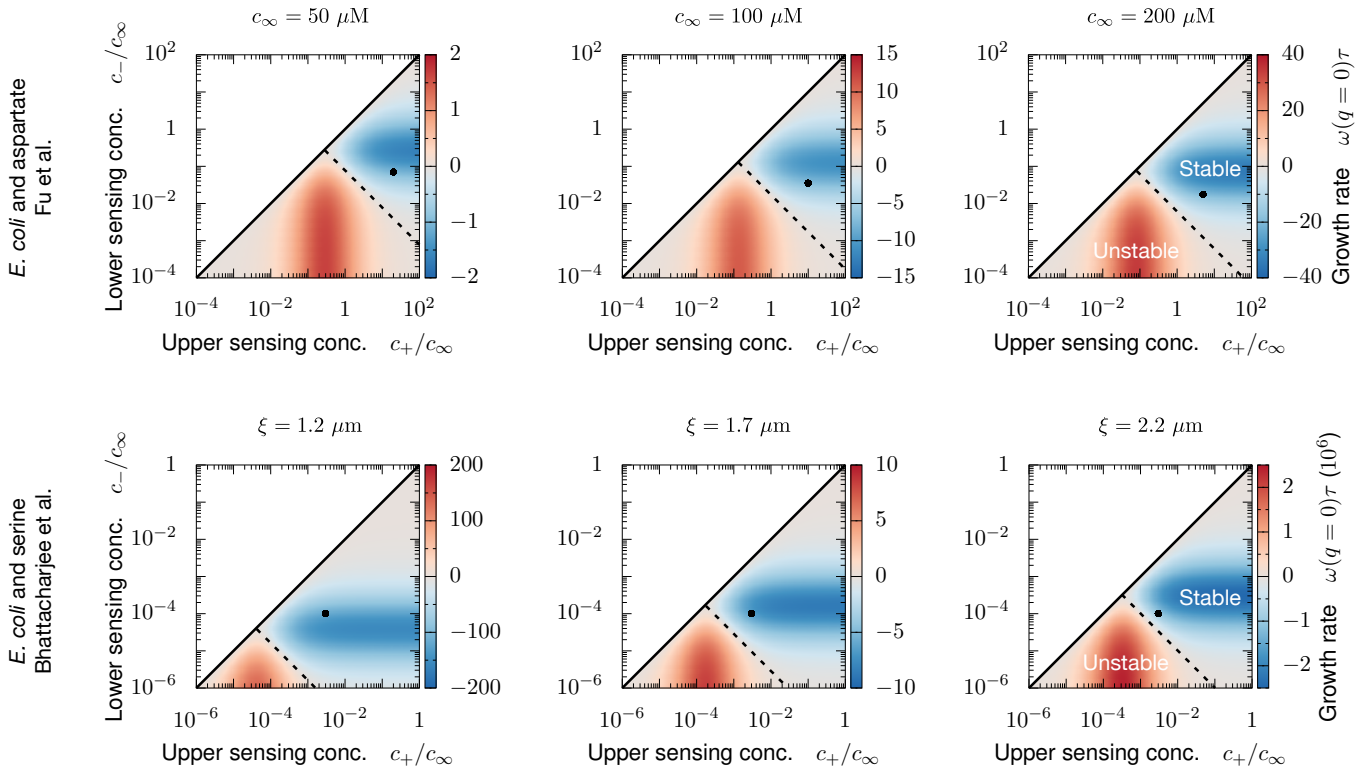


Figure S4 | Stability of chemotactic fronts of *E. coli* in experiments. In the experiments by Fu et al.¹⁷, *E. coli* swim in liquid media with three different initial concentrations c_∞ of the chemoattractant aspartate. In the experiments by Bhattacharjee et al.²⁰, *E. coli* swim through porous media of three different pore sizes ξ . For each experiment, the stability diagram is plotted using the parameter values in Table II. The points correspond to the actual experimental conditions, namely the values of c_+/c_∞ and c_-/c_∞ in each case. In all cases, our analysis predicts stable fronts, consistent with the experimental observation of flat fronts.